Microchimica Acta (2023) 190:61
https://doi.org/10.1007/s00604-022-05629-3

ORIGINAL PAPER

# Chiral template–induced porphyrin-based self-assembled materials for electrochemical chiral sensing

Xiaohui Niu[1] · Simeng Yan[1] · Rui Zhao[1] · Sha Han[1] · Kunjie Cao[1] · Hongxia Li[1] · Kunjie Wang[1]

Received: 9 September 2022 / Accepted: 17 December 2022 / Published online: 20 January 2023


## Abstract

Chirality plays a key role in many fields of natural sciences as well as life sciences. Chiral materials are widely developed and used for electrochemical chiral recognition. In recent years, carbon quantum dots (CQDs) have been widely used as a novel carbon nanomaterial due to their excellent charge transfer properties, good biocompatibility, and low cost. The special structure of π-conjugated porphyrin attracts attention. Supramolecular self-assembly shows a way to construct chiral materials by self-assembling simple molecules into chiral composites. Herein, we demonstrate the self-assembly of achiral porphyrins induced by chiral carbon quantum dots assembled from L- and or D-tryptophan (L- and or D-Trp) with carbon quantum dots, resulting in 5,10,15,20-tetrakis (4-carboxyPheyl) (TCPP) self-assembled structure. The electrochemical chiral recognition of chiral self-assembled materials was studied using Phenylalanine (Phe) enantiomer as a chiral analyte. Electrochemical chiral recognition results showed that the chiral self-assembled materials induced by chiral templates have a good ability to discriminate Phe enantiomers. Therefore, this research provides a new idea for the synthesis of chiral composites and further expands applications to electrochemical chiral recognition.

**Keywords** Template method · Chiral induction · Self-assembly · Chiral materials · Electrochemical recognition

## Introduction

Chirality is an impressive characteristic of asymmetric structures to explain two mirror-image forms [1]. Except for glycine, other amino acids have two different configurations (L- and D-form) due to the chiral carbon atoms [2, 3]. Since chiral molecules with different configurations may have different or even opposite effects, the identification of chiral molecules is of great significance in the field of life sciences [4, 5]. Therefore, the enantioselective recognition of chiral molecules is especially important in the fields of pharmaceutics, food science, and life science [6]. In the past decades, many techniques, such as circular dichroism spectroscopy [7, 8], colorimetric analysis [9], capillary electrophoresis [10, 11] and high performance liquid chromatography (HPLC) [12], have been proposed to discriminate chiral isomers. However, traditional methods of identifying chiral molecules have many disadvantages, such as tedious operations, time-consuming and labor-intensive, and expensive chiral stationary phases. All these disadvantages limit their application in chirality related fields [13]. In the latest research, electrochemical technology is widely used in the field of analytical chemistry due to its advantages of rapid detection, high sensitivity and low price [14].

The self-assembly method has broad application prospects in the synthesis of chiral materials. The properties of chiral materials are not only related to their own molecular structure, but also to the self-assembly process [15]. Interestingly, both chiral and achiral molecules may self-assemble to construct chiral composites by regulating conditions [16]. Therefore, elucidating the self-assembly mechanism of chiral self-assembled materials is indispensable in life science and other fields. Wu and co-workers [17] reported a simple chirality transfer strategy, which makes achiral glycine (Gly) with chirality. This work successfully prepared CuO (L-CuO) with chirality for the first time, which can be used to detect chiral molecules by forming $Cu(Gly)_2$ complexes. Chirality transfer strategy from optically active L-CuO to

✉ Xiaohui Niu
18893700891@163.com

✉ Kunjie Wang
wangkj80@163.com

[1] College of Petrochemical Technology, Lanzhou University of Technology, 730050 Lanzhou, People's Republic of China

glycine was further verified by circular dichroism (CD) spectroscopy.

Due to their good biocompatibility, low toxicity, luminescence, size effect, and photoinduced electron transfer properties, carbon quantum dots (CQDs) have broad application prospects in many fields. In past research, great progress has been made in the synthesis and application of carbon quantum dots. In addition, due to its more reactive sites, carbon quantum dots have also been reported and studied in the related fields of chiral materials. It has been applied in electrochemical chiral recognition biomolecules and showed good recognition efficiency. The chiral counterparts of the chiral material is attached to a left-handed or right-handed chiral site [18]. Zhang and co-workers [19] synthesized chiral carbon quantum dots by hydrothermal method using citric acid (CA) and left- or right-handed cysteine as raw materials. Wei et al. [20] reported one-step synthesis of chiral CQDs by using L-/D-tryptophan (L-/D-Trp) as carbon source and chirality source, which has chirality, fluorescence and biocompatibility. The synthesis of chiral carbon quantum dots is simple and has many active sites, which can provide a sensing platform for chiral molecules, but the limitations of chiral carbon quantum dots themselves cannot achieve a good recognition effect.

Porphyrin represents one of the most widely studied of all known macrocyclic ring systems [21, 22]. Porphyrins are a class of macromolecular heterocyclic compounds formed by the interconnection of the α-carbon atoms of four pyrrole-like subunits through a methine bridge [23, 24]. 5,10,15,20-tetrakis(4-carboxyPheyl)porphyrin (TCPP) is a relatively common porphyrin compound with stable structure and strong polarity, which is shown in Fig. S1. In previous studies, self-assembled nanomaterials based on porphyrins have been used in sensors, especially in nonlinear optical devices, and photoelectronics [25, 26]. Jaecheol Choi and co-workers [27] fabricated a self-assembled electrocatalyst material for $CO_2$ reduction, which formed a self-assembled structure through the π-π interaction and electrostatic interactions between reduced graphene oxide frameworks (FePGFs) and 5,10,15,20-tetrakis(4-trimethylammoniumPheyl) porphyrin to iron(III) pentachloride. However, there are few studies on chiral materials of porphyrins, which may be related to the achiral properties of porphyrins [28]. Fortunately, achiral porphyrin-based molecules can be induced to endow chirality through self-assembly with chiral materials, which provided an idea for the fabrication of chiral materials by transfer of chirality to achiral molecules via template induction via self-assembly. Chen et al. have synthesized 5,10,15,20-tetrakis (4-carboxyPheyl) porphyrin (TCPP)/N-(4-Aminobenzoyl)-L-glutamic acid diethyl ester (L-GDE) chiral materials (TCPP/L-GDE) via self-assembly, which has different self-assembled structures. The above elaboration proves that porphyrin-based materials can self-assemble with chiral molecules or other molecules through non-covalent forces [29]. In this work, chiral carbon quantum dots were first synthesized to form amide bonds via CQDs and L-Trp or D-Trp, the addition of EDC and NHS activates the functional groups of L-Trp and D-Trp, and combines with the carboxyl groups at the edge of CQDs through amination reaction to form chiral carbon quantum dots (Scheme 1a). Then, the achiral TCPP was induced to produce chirality by self-assembly using *L*-CQDs and *D*-CQDs as templates, a chiral material based on TCPP is synthesized (*L*-CQDs/TCPP and *D*-CQDs/TCPP) (Scheme 1b), which is applied for identification of Phe isomers. TCPP is bound to chiral carbon quantum dots through a variety of intermolecular forces, mainly hydrogen bonding force and π-π interaction between the benzene ring and the pyrrole ring. *L*-CQDs/TCPP and *D*-CQDs/TCPP were used for stereoselective recognition of Phenylalanine (Phe) isomers via electrochemical methods, due to electrochemical methods can convert invisible forces between chiral host and chiral guest into obvious electrochemical signals (Scheme 1c).

## Experimental

### Materials

5,10,15,20-tetrakis(4-carboxyPheyl) porphyrin (TCPP), D-Phenylalanine and L-Phenylalanine were purchased from SAIN Chemical Technology (Shanghai) Co., Ltd. L-tryptophan, D-tryptophan were obtained from Shanghai Aladdin Chemical Co., Ltd. Disodium phosphate ($Na_2HPO_4{\cdot}12H_2O$), Sodium dihydrogen phosphate ($NaH_2PO_4{\cdot}12H_2O$), and Potassium chloride (KCl) were purchased from Tianjin Damao Chemical Reagent Co., Ltd. Potassium ferricyanide [$Fe(CN)_6^{3-}$] were purchased from Beijing chemical plant. Potassium ferrocyanide [$Fe(CN)_6^{4-}$)] were purchased from Sinopharm Chemical Reagent Co., Ltd.

### Apparatus

Fourier transform infrared (FT-IR) spectra of all materials were recorded on spectrophotometer (IEC/CN 60,825–1:2007) using KBr pellets with the range change from 4000 to 500 $cm^{-1}$. X-ray photoelectron spectroscopy (XPS) of different materials was measured on a ThermoFisher Scientific X-ray photoelectron spectrometer (ESCALAB 250 Xi). X-ray diffraction (XRD) of different materials was carried out on an X-ray diffractometer (PANalytical X'PERT PRO). All electrochemical tests including cyclic voltammetry (CV), differential pulse voltammetry (DPV) and electrochemical impedance spectroscopy (EIS) were performed on a Shanghai Chen Hua CHI600E

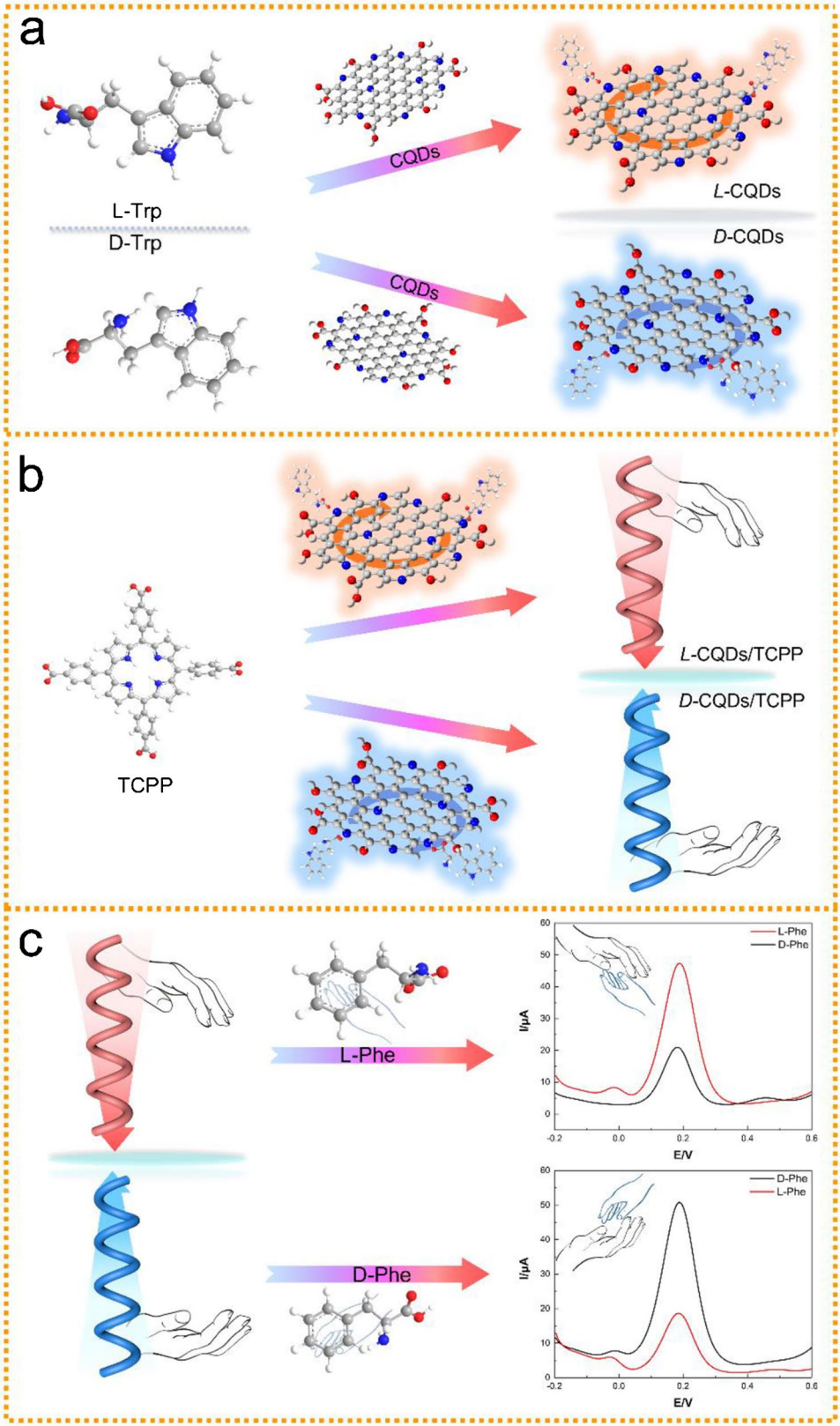


**Scheme 1** (**a**) synthesis of chiral templates (**b**) synthesis of composites (**c**) schematic diagram of chiral recognition

electrochemical workstation. Bare or modified glassy carbon electrodes (GCE) were used as working electrodes. A platinum wire was used as the counter electrode. A saturated calomel electrode was used as the reference electrode.

### Preparation of chiral template material

CQDs were synthesized with sodium citrate and urea as carbon sources. 2.5 g of citric acid and 2.16 g of urea were dissolved in 60 mL of deionized water and stirred thoroughly. The above solution was put into a 100 mL reactor and reacted at 160 °C for 4 h. Add 300 mL of ethanol and let stand for 30 min. The precipitate was dialyzed, centrifuged and freeze-dried to obtain CQDs. The synthesis of chiral CQDs was carried out at room temperature with L and D-tryptophan as the chiral source, respectively. Firstly, 25 mg of EDC was added to 25 mL of uniformly dispersed CQDs (2 mg $mL^{-1}$) dispersions. After stirring for 10 min, 25 mg of NHS was added to the above-mentioned dispersion and stirred for 30 min. Then, 50 mg of L-Trp or D-Trp were dispersed in 25 mL of ultrapure water and sonicated for 20 min, respectively. Then, L or D-Trp solution was added dropwise to the above solution for over 30 min and continued vigorous stirring for 4 h. The above solution was dialyzed for 48 h, and then freeze-dried to obtain the chiral CQDs templates (*L*-CQDs and *D*-CQDs).

### *Chirality induction* via *self-assembly*

TCPP self-assembly was induced by self-assembly through π-π and hydrogen bonding interactions by using the above synthesized *L*-CQDs and *D*-CQDs as chiral template, respectively. 10 mg of TCPP and 10 mg of *L/D*-CQDs were dissolved in 20 mL of ultrapure water and heated to 60 °C and reacted for 30 min, then cooled to room temperature and stirred for 24 h to obtain *L*-CQDs/TCPP and *D*-CQDs/TCPP.

## Results and discussion

### Characterizations

The XPS surveys can give us a deeper understanding of the chirality-induced effect of *L/D*-CQDs on TCPP through self-assembly. As shown in Fig. S2a and b, the wide XPS spectra of *L*-CQDs/TCPP and *D*-CQDs/TCPP exhibited three characteristic peaks appeared at C 1 s (284.6 eV), N 1 s (397.5 eV) and O 1 s (529 eV), respectively. C mainly comes from benzene ring and pyridine ring. N mainly comes from nitrogen-doped carbon quantum dots, in the pyridine ring and amino of Trp and O mainly comes from Trp and carboxyl groups on TCPP. Atomic % of XPS at Table S1.

The C1s spectrum can be fitted into four main peaks at 288.9 eV of C = O, 287.4 eV of C-N, 286.1 eV of C-O and 284.8 eV of C = C/C–C, respectively (Fig. 1a). Another four peaks of C 1 s are found in *D*-CQDs/TCPP at 288.8, 287.5, 286.2 and 284.8 eV corresponded to C = O, C–N, C-O and C = C/C–C, respectively (Fig. 1d). The N 1 s XPS spectrum of *L*-CQDs/TCPP can be divided into three bands with the binding energy of 397.9, 400.1, and 402.2 eV, which originated from -C-$NH_2$, pyrrole N, and carbon quantum dots doped with N, respectively (Fig. 1b). The N 1 s XPS spectrum of *D*-CQDs/TCPP can also be divided into three bands with typical characteristic peaks of 402.1, 400.0, and 397.8 eV, which originated from carbon quantum dots doped with N, Pyrrole N, and -C-$NH_2$, respectively (Fig. 1e). The high resolution of the O1s showed in Fig. 1c with two peaks at 531.8 and 533.6 eV, which can be fitted with -C–OH and C = O groups. As shown in Fig. 1f, the two peaks of *D*-CQDs/TCPP at 531.9 and 533.6 eV were attributed to -C–OH and C = O. XPS spectrum analysis proves that the successful self-assembly of *D*-CQDs/TCPP and *L*-CQDs/TCPP was induced by chiral templates.

As shown in Fig. 2a, the stretching vibrational peaks of *L*-CQDs and *D*-CQDs at 1593 and 1589 $cm^{-1}$, respectively, are considered to be C = O in the amide II band. This is due to the fact that carbon quantum dots contain a large number of carboxyl groups that undergo amidation reactions with -$NH_2$ on L-Trp and D-Trp to form amide bonds. TCPP shows a typical characteristic peak at 1686 $cm^{-1}$, which is attributed to the C = O stretch in Fig. S3. In order to further explore the crystal structure of the different materials, the XRD test was also carried out. As shown in Fig. 2c, the XRD curves of *L*-CQDs and *D*-CQDs all showed a large bag peak at 20–30°, which is the amorphous peak of carbon. The XRD pattern of TCPP shows a characteristic peak at 2θ = 6.3° in the low-angle range, which belongs to the (100) plane (Fig. S4). In the wide-angle region, the characteristic diffraction peaks appeared at 2θ = 20°, which is attributed to (300) lattice planes. Besides, the sharp peak at 2θ = 26° can be ascribed to the stacking distance between neighboring porphyrin rings along the direction perpendicular to the porphyrin rings. As shown in Fig. 2d, After *L*-CQDs and *D*-CQDs were synthesized by self-assembly, the XRD pattern of *L*-CQDs and *D*-CQDs not only shows the peaks of TCPP, but also contains the peaks of *L*-CQDs and *D*-CQDs. The TEM image demonstrates that as-synthesized CQDs exhibited good dispersion with average particle size of 2.5 ± 0.5 nm in diameter (Fig. S6). When chiral materials are synthesized by self-assembly, as shown in Fig. 2e and f the SEM image demonstrates that the two materials show the same elongated appearance, and the diameter of *D*-CQDs/TCPP is wider than that of *L*-CQDs/TCPP under the same magnification, this is because the different steric conformations of *L*-CQDs and *D*-CQDs have different forces on

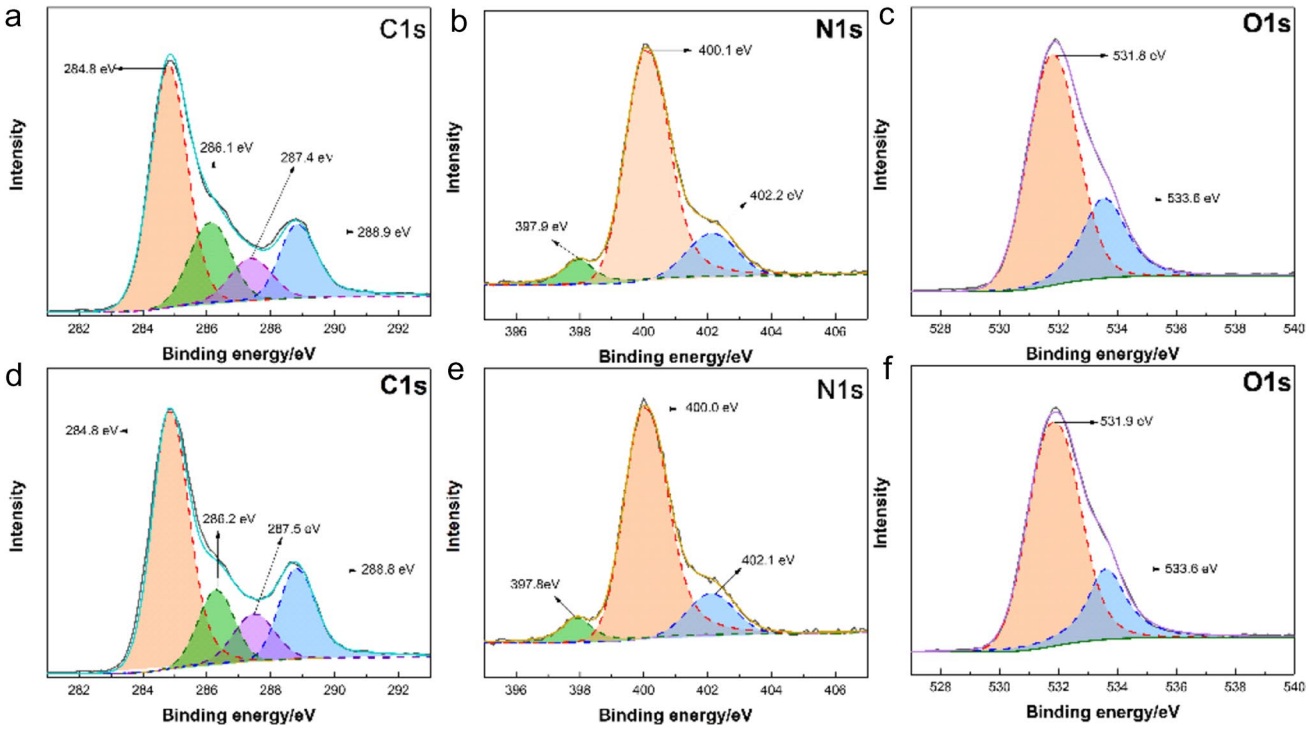


**Fig. 1** (**a**) High resolution C 1 s XPS, (**b**) N 1 s XPS, (**c**) O 1 s XPS spectra of *L*-CQDs/TCPP, (**d**) high resolution C 1 s XPS, (**e**)N 1 s XPS (**f**)O 1 s XPS spectra of *D*-CQDs/TCPP

TCPP during self-assembly. As a result, the chiral composites synthesized by induction have different sizes. Similar results were obtained in previous reports by Shanshan Wu and co-workers [30]. It is proved that when TCPP interacts with different configurations of lysine, one configuration of chiral composites is nanofiber and the other is willow leaf.

## Electrochemical properties of different modified electrodes

The CVs of different materials modified electrodes were measured in 0.1 M KCl containing 5 mM Fe $(CN)_6^{4-/3-}$, which are shown in Fig. 3a. Due to the conversion between Fe $(CN)_6^{4-}$ and $Fe(CN)_6^{3-}$, a well-defined oxidation peak and reduction peak appear at all the tested systems. The redox peak of CQDs/GCE was smaller than the bare GCE, which is because the carboxyl and hydroxyl groups of CQDs are electron rich, which will cause electrostatic repulsion with $Fe(CN)_6^{4-}$ and $Fe(CN)_6^{3-}$ in the solution, resulting in lower peak current than the bare electrode. Similarly, the electrochemical response of the TCPP/GCE was also lower than that of the naked electrode. The peak current of TCPP/GCE is significantly reduced compared with naked GCE, which can be attributed to the strong electrostatic repulsions between the highly electronegative carboxyl groups of TCPP and the $Fe(CN)_6^{4-/3-}$ probe in the solution. We can see from the Fig. S7a that the redox peak of *L*-CQDs/GCE is smaller than that of *D*-CQDs/GCE, but both are lower than naked electrode, which may be due to the difference in electron transfer at the sensing interface due to the steric hindrance of Trp (corresponding to the EIS Figure). It is worth noting that the peak current value of *L/D*-CQDs/TCPP/GCE is smaller than that of CQDs/GCE but higher than that of TCPP/GCE, which further indicates the successful recombination of the material. The EIS spectra of *L*-CQDs/GCE and *D*-CQDs/GCE are exhibited in Fig. 3b. It can be observed from the EIS of other modified electrodes (Fig. S7b and Fig. 3b), the charge-transfer resistance ($R_{ct}$), it can be seen from the impedance semicircle in the high-frequency region, the order of the charge-transfer resistance (Rct) is GCE < CQDs/GCE < *D*-CQDs/TCPP/GCE < *D*-CQDs/GCE < *L*-CQDs/TCPP/GCE < *L*-CQDs/GCE < TCPP/GCE. The results of EIS are consistent with CV.

The different scanning speeds of *L*-CQDs/TCPP/GCE and *D*-CQDs/TCPP/GCE were tested to investigate the dynamics of the electrode reaction. It can be seen from Fig. 3c and d that when the scan rate increased from 10 to 100 mV $s^{-1}$, the anodic peak shifts to positive potential and the cathodic peak shifts to negative potential. From Fig. 3e and f, it can be seen that the *L*-CQDs/TCPP/GCE and *D*-CQDs/TCPP/GCE peak currents have a linear relationship with the square root of the scan velocity, showing that the electrochemical process is diffusion-controlled. The linear equation of *L*-CQDs/TCPP is $I_{pa} = 1.97v^{1/2} - 1.50$

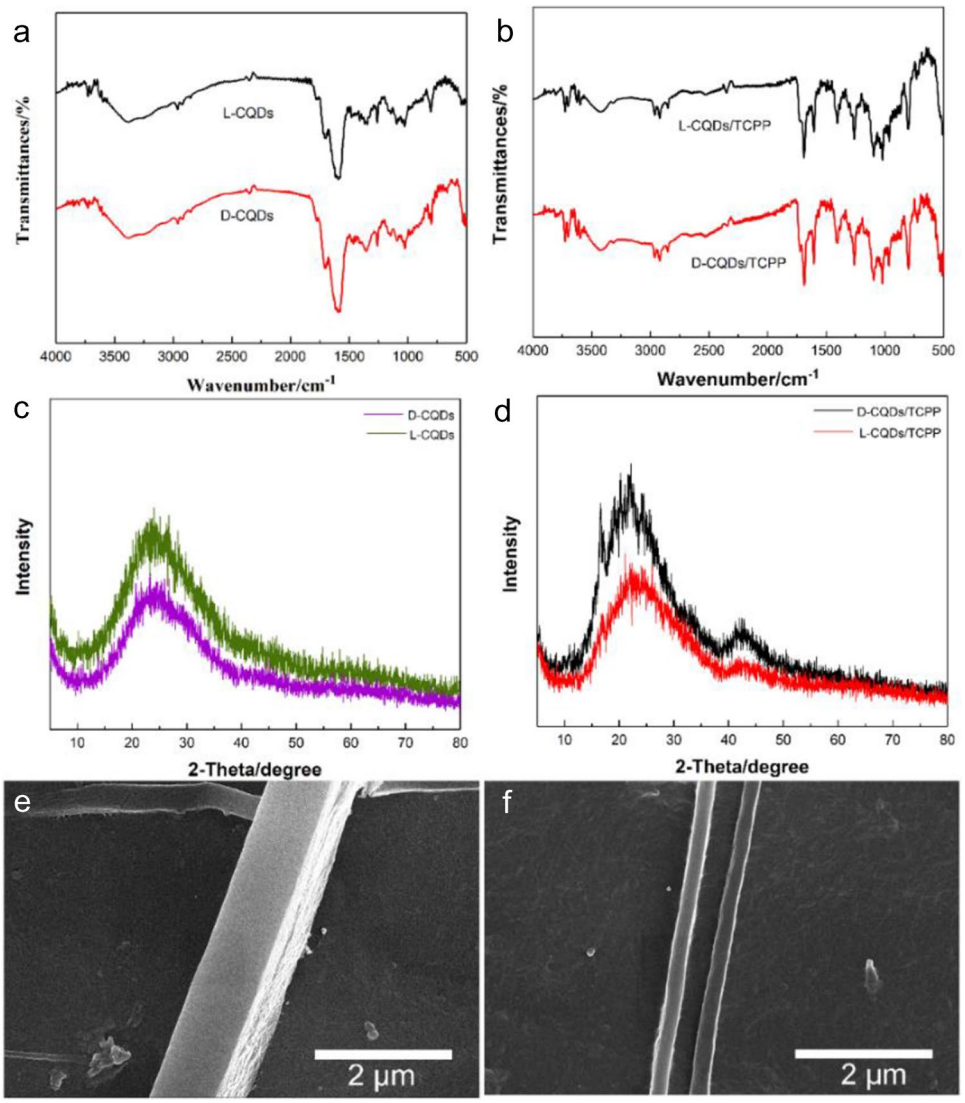


**Fig. 2** (**a**) and (**b**) FI-IR of different composite materials, XRD of different composite materials (**c**) and (**d**); (**e**) SEM image of *D*-CQDs/TCPP; (f) SEM image of *L*-CQDS/TCPP

($R^2 = 0.934$) and $I_{pc} = -1.43v^{1/2} + 1.37$ ($R^2 = 0.883$). The linear equation of *D*-CQDs/TCPP can be represented as $I_{pa} = 1.77v^{1/2} - 3.57$ ($R^2 = 0.940$) and $I_{pc} = -1.33v^{1/2} + 2.74$ ($R^2 = 0.935$).

## Chiral materials distinguish the corresponding isomers of Phe

In order to compare the chiral recognition ability of different chiral materials, the DPV test was used to reflect the invisible recognition force between chiral materials and chiral guests to electrochemical signals, thereby generating a visual chiral recognition signal. From Fig. 4a and b, when *D*-CQDs/GCE and *L*-CQDs/GCE were used to recognize L-Phe and D-Phe, the peak current ratios $I_{D\text{-}Phe}/I_{L\text{-}Phe} = 1.6$ and $I_{L\text{-}Phe}/I_{D\text{-}Phe} = 1.7$, respectively, indicating that *L/D*-CQDs almost has no recognition effect on L/D-Phe. Although the *D*-CQDs and *L*-CQDs have chiral environment, it cannot effectively distinguish the Phe isomers during the recognition process. This may be due to the weak force and less steric hindrance between chiral recognition sites and L-Phe and D-Phe, so the two enantiomers cannot be distinguished by *D*-CQDs/GCE and *L*-CQDs/GCE. Fortunately, the chiral recognition effect is increased obviously on the chiral materials induced by chiral templates of *D*-CQDs/TCPP/GCE ($I_{D\text{-}Phe}/I_{L\text{-}Phe} = 2.7$, Fig. 4c) and *L*-CQDs/TCPP/GCE ($I_{L\text{-}Phe}/I_{D\text{-}Phe} = 2.3$, Fig. 4d). It can be seen that the introduction of TCPP plays a non-negligible role in improving the recognition effect of self-assembled chiral materials. The self-assembly of TCPP and chiral template not only increased the recognition sites of the composites, but also produced a large steric hindrance effect, which made it possible to achieve a better differentiation effect for L-Phe and D-Phe. It is worth noting that the chiral recognition efficiency of *D*-CQDs/TCPP/GCE is slightly better than that of *L*-CQDs/TCPP/GCE (2.7vs2.3), which may be caused by the different micromorphology of

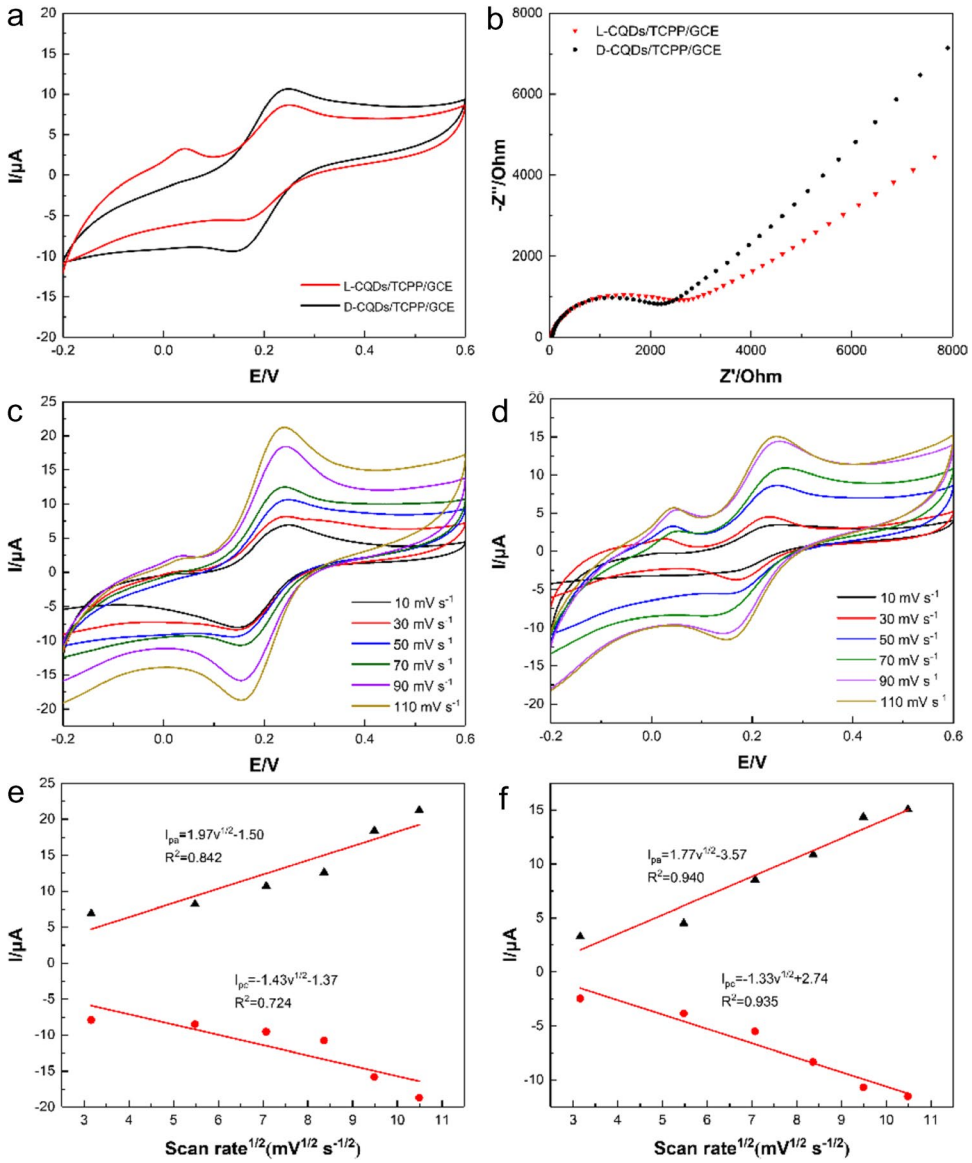


**Fig. 3** The CVs (**a**) *L*-CQDs/TCPP and *D*-CQDs/TCPP (**b**) EIS of *L*/*D*-CQDs/TCPP. (**c**) and (**d**) CVs of *L*-CQDs/TCPP and *D*-CQDs/TCPP at increasing scan reates. (**e**) and (**f**) Linear relationship between cathode and anode peak current and scanning rate of *L*-CQDs/TCPP and *D*-CQDs/TCPP

*L*-CQDs/TCPP and *D*-CQDs/TCPP during the self-assembly process. We have compared the existing reports and highlight the advantages of the materials with the report in Table S2. The results show that the recognition efficiency of this work is better than or equivalent to other work.

To explore in-depth the chiral recognition effect of the chiral composites with different configurations for chiral molecules of the same configuration, *D*-CQDs/GCE and *L*-CQDs/GCE were immersed in L-Phe and D-Phe to test its DPV. It can be seen from Fig. 5a and b that the peak current ratio of $I_{D\text{-CQDs/GCE}}/I_{L\text{-CQDs/GCE}}$ in L-Phe and D-Phe are 1.8 and 1.6, respectively. Although *L*-CQDs and *D*-CQDs are chiral and have chirality and have recognition sites, neither *L*-CQDs and *D*-CQDs in L-Phe solution, nor *L*-CQDs and *D*-CQDs in D-Phe solution, have much difference in peak current. Even if the recognition effect is poor, it can be seen from the peak current value that *L*-CQDs has a strong binding ability to D-Phe, and *D*-CQDs has a strong force to L-Phe. However, as shown in Fig. 5c and d, the peak current ratio of *D*-CQDs/TCPP/GCE and *L*-CQDs/TCPP/GCE in L-Phe and D-Phe is 2.6 and 2.3, respectively. The result indicates that the chiral composites formed by self-assembly have stronger binding force to the chiral guest molecules due to their more chiral recognition sites. Similarly, it can be seen from the DPV curve that *L*-CQDs/TCPP/GCE has a higher binding capacity to D-Phe, and *D*-CQDs/TCPP/GCE has a higher binding capacity to L-Phe. Similarly, we can observe from the DPV curve that *L*-CQDs/TCPP/GCE has a high binding capacity to D-Phe and *D*-CQDs/TCPP/GCE has a high binding capacity to L-Phe, which indicates that

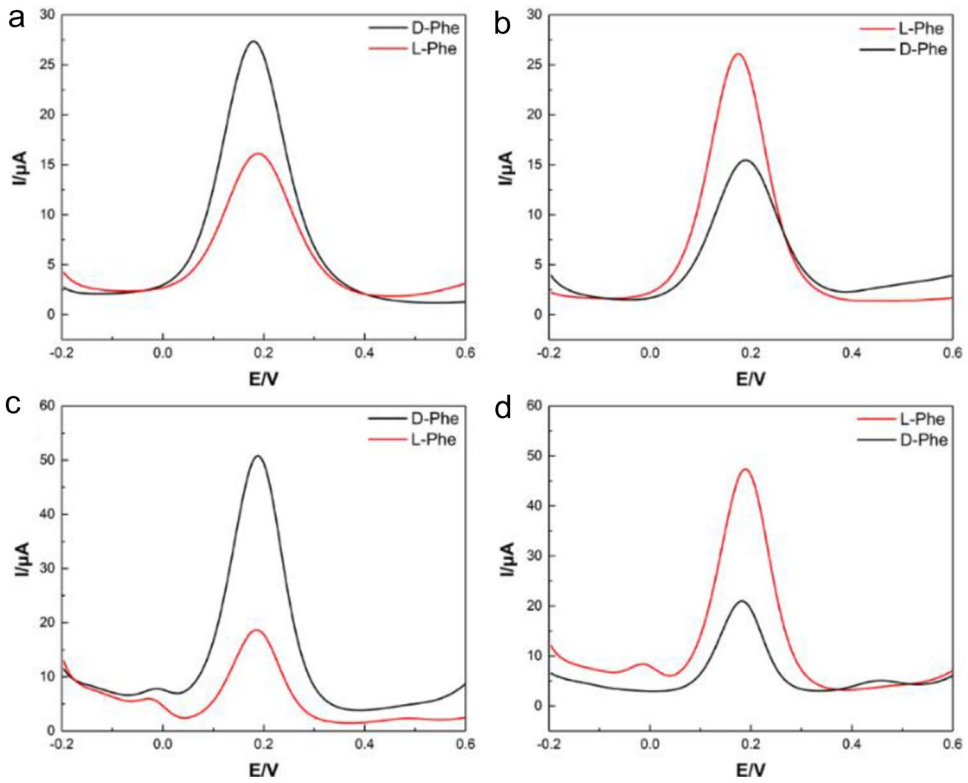


**Fig. 4** (**a**) and (**b**) are the peak current of *D*-CQDs and *L*-CQDs to L/D-Phe, (**c**) and (**d**) are the peak current of *D*-CQDs/TCPP and *L*-CQDs/TCPP to L/D-Phe

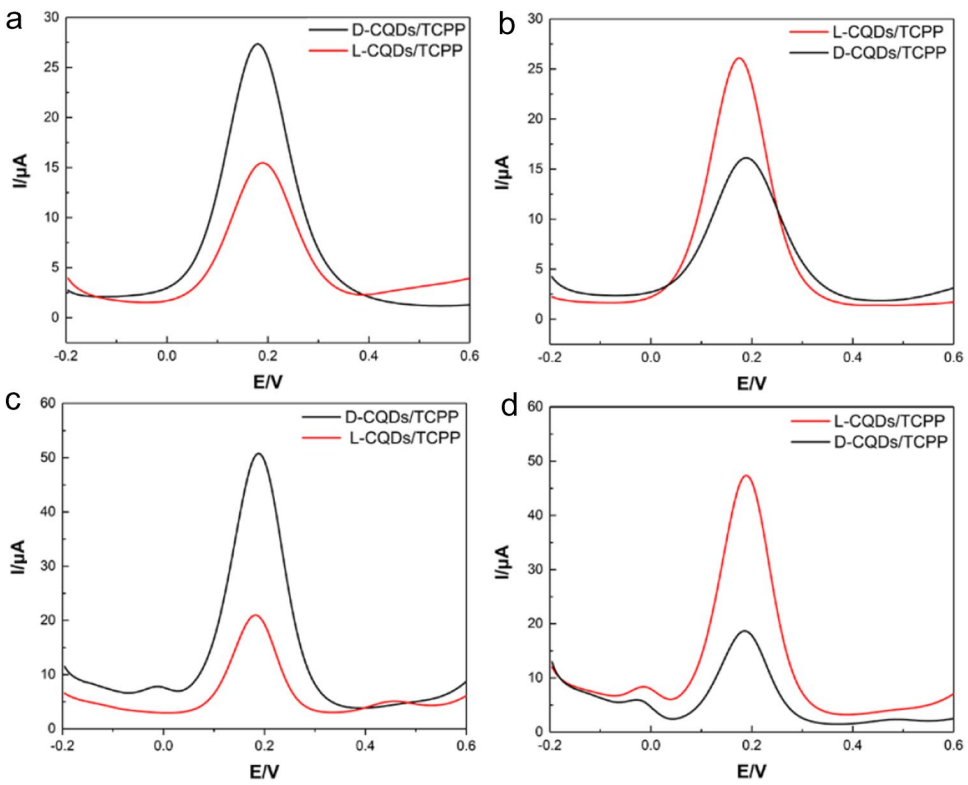


**Fig. 5** (**a**) and (**b**) the peak current of *L*-CQDs and *D*-CQDs to D-Phe and L-Phe, (**c**) and (**d**) the peak current ratio of *L*-CQDs/TCPP and *D*-CQDs/TCPP to D-Phe and L-Phe

the self-assembled chiral host and chiral guest form diastereomers to produce chiral recognition.

## Concentration optimization

In order to obtain better recognition effect, it is of importance to explore the experiment conditions for the recognition of Phe isomers. Firstly, the effect of Phe isomer concentration on the DPV peak current responses of *D*-CQDs/TCPP/GCE and *L*-CQDs/TCPP/GCE was studied respectively, which is closely related to the electrochemical response signal of the electrochemical sensing interface. From Fig. 6a and b, it can be seen that the peak currents of *D*-CQDs/TCPP/GCE for L-Phe and D-Pen increased with increasing concentrations from 1 to 6 mM and increases linearly. The linear regression equations of *D*-CQDs/TCPP/GCE for L-Phe and D-Phe concentration are $\Delta I = 4.52 + 26.29C_D$ ($R^2 = 0.962$) and $\Delta I = 0.68 + 15.30C_L$ ($R^2 = 0.948$), respectively (Fig. 6c). As seen in Fig. 6c and d, the peak current value increases with the increase of L-Phe and D-Phe concentrations in the electrochemical test of Phe isomers by *L*-CQDs/TCPP/GCE. The linear regression equations for the change of Phe isomer concentration are $\Delta I = 4.28 + 25.87C_L$ ($R^2 = 0.975$) and $\Delta I = 1.71 + 13.78C_D$ ($R^2 = 0.968$), respectively (Fig. 6f). In addition, it can be seen on *L*-CQDs/TCPP/GCE that the peak current of L-Phe is always higher than that of D-Phe. This is consistent with the previous electrochemical chiral recognition results.

## Interference test

In addition, the anti-interference ability of the chiral sensing interface was also evaluated by the addition of interfering ions ($Co^{2+}$, $Zn^{2+}$, $Cu^{2+}$) and small organic molecules

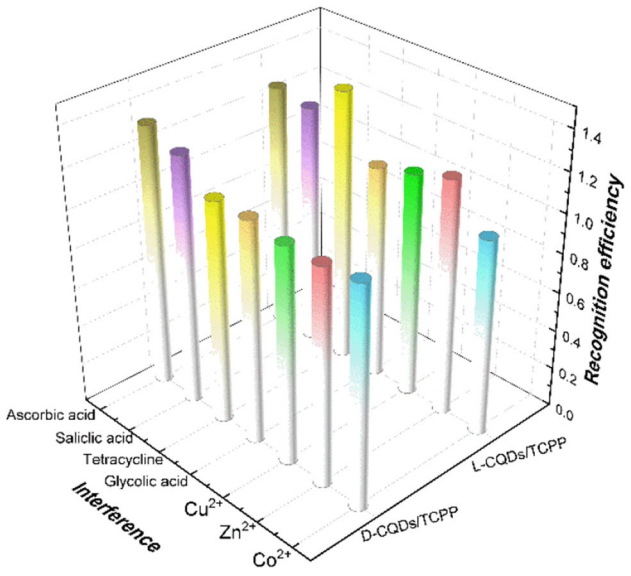


**Fig. 7** The anti-interference of ions and organics

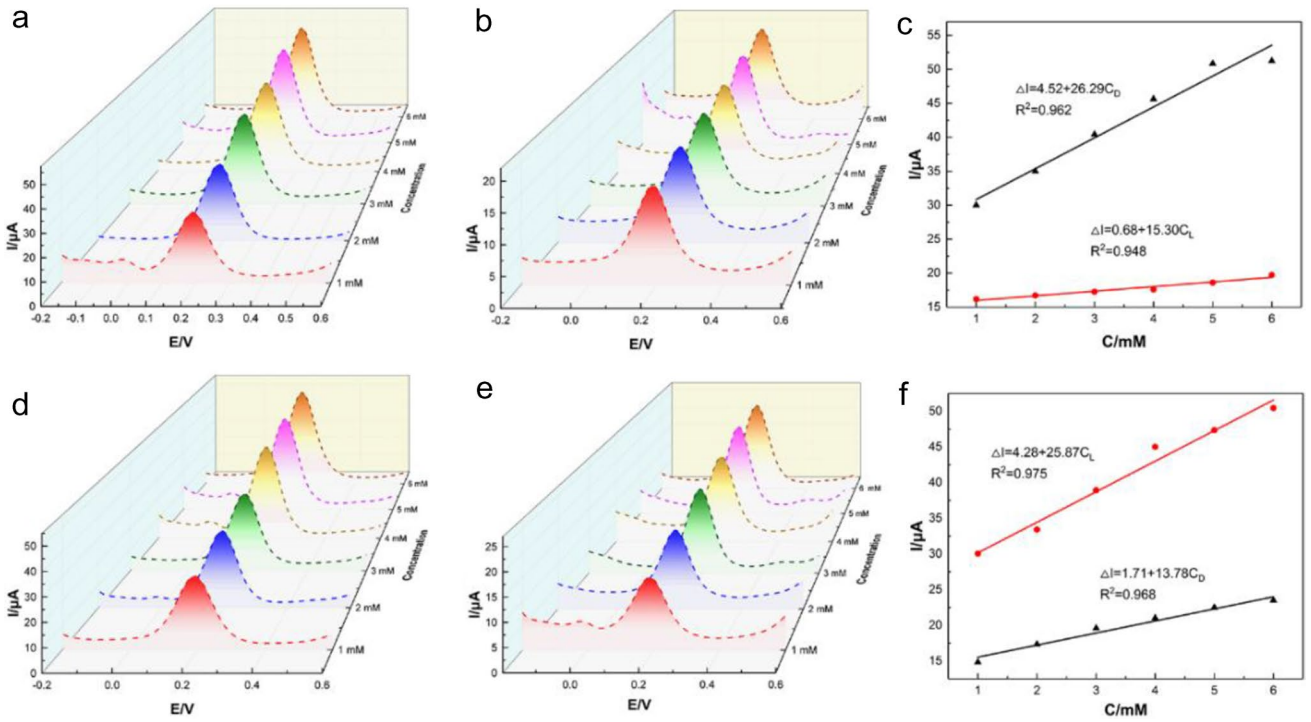


**Fig. 6** (**a**) and (**b**) The DPV of *D*-CQDs/TCPP in L-Phe and D-Phe with the increase of concentration. (**c**) Linear relationship between peak current of *L*-CQDs/TCPP (**d**) and (**e**) The DPV of *L*-CQDs/TCPP in D-Phe and L-Phe with the increase of concentration. (**f**) Linear relationship between peak current of *L*-CQDs/TCPP.

(glycolic acid, tetracycline, salicylic acid, ascorbic acid). It can be observed from Fig. 7 that the addition of the metal ions with strong coordination ability, such as $Co^{2+}$, $Zn^{2+}$, $Cu^{2+}$, will weaken the ability of *L/D*-CQDs/TCPP/GCE to recognize Phe enantiomers. This may be because these ions with strong coordination ability can coordinate with chiral host materials and chiral guest molecules to occupy their active sites. Thus, diastereomers are not easily formed between *L*-CQDs/TCPP and D-Phe, and *D*-CQDs/TCPP and L-Phe. Some small organic molecules, such as glycolic acid, tetracycline, salicylic acid and ascorbic acid were also introduced in anti-interference studies. As shown in Fig. 7, these organics have a great influence on the results of chiral recognition. This is because the addition of these small organic molecules introduces active sites and interferes with the binding between host and guest.

## Actual sample test

Phenylketonuria (PUK) [31], caused by abnormal phenylalanine metabolism in the body, is one of the few congenital genetic diseases that can be diagnosed and treated early. Therefore, we detected L-Phe in normal serum and PUK patient serum, as well as normal infant serum and PUK infant serum by standard addition method [32].

When *L*-CQDs/TCPP is used to detect L-Phe in adult samples (Table 1), the experimental results show that the recovery rate in normal serum is 29.5–40.1%, and the recovery rate in normal infant serum is 31.9–42.6%. The recovery rate in the serum of PUK patients ranged from 35.1 to 42.5%, and the recovery rate in the serum of PUK infant patients ranged from 29 to 41.7%. When *L*-CQDs/TCPP is used to detect L-Phe in the infant sample (Table 2), the recovery ranged from 29 to 42.5%, indicating that the detection of L-Phe in the actual sample by *L*-CQDs/TCPP was consistent with the previous electrochemical data, and *L*-CQDs/TCPP could not form a stable structure with the same chiral L-Phe.

When *D*-CQDs/TCPP is used to detect L-Phe in adult samples (Table 3), the experimental results show that the recovery rate in normal serum is 94.6–102.0%, and the recovery rate in normal infant serum is 95.5–102.0%. The recovery rate in the serum of PUK patients ranged from 97.5 to 103.1%, and the recovery rate in the serum of PUK infant patients ranged from 95.2 to 102.4%. When *D*-CQDs/TCPP is used to detect L-Phe of infant samples (Table 4), the recovery ranged from 94.6 to 103.1%, indicating that *D*-CQDs/TCPP and L-Phe can form a stable diastereomeric structure, which corresponds to the previous electrochemical test.

**Table 1** Determination of L-Phe in serum. Determination of L-Phe in adult serum by *L*-CQDs/TCPP (n = 4)

| Sample | CL[a] (μM) | Added (μM) | Founded (μM) | Recovery (%) |
|---|---|---|---|---|
| Normal serum | 50.5 | 0.5 | 15.03 ± 0.27 | 29.5 |
| | | 1.0 | 21.06 ± 0.42 | 40.1 |
| | | 10.0 | 18.58 ± 0.56 | 30.7 |
| | | 50.0 | 38.39 ± 1.51 | 38.2 |
| PUK patient serum | 1000.5 | 0.5 | 351.2 ± 0.09 | 35.1 |
| | | 1.0 | 425.9 ± 0.27 | 42.5 |
| | | 10.0 | 407.6 ± 0.45 | 40.3 |
| | | 50.0 | 421.4 ± 2.51 | 40.1 |

[a] Content of L-Phe in the sample.

**Table 2** Determination of L-Phe in infant serum. Determination of L-Phe in infant serum by *L*-CQDs/TCPP (*n* = 4)

| Sample | CD[b] (μM) | Added (μM) | Founded (μM) | Recovery (%) |
|---|---|---|---|---|
| Normal infant serum | 40.3 | 0.5 | 17.4 ± 0.26 | 42.6 |
| | | 1.0 | 13.2 ± 0.38 | 31.9 |
| | | 10.0 | 21.3 ± 0.55 | 42.3 |
| | | 50.0 | 29.1 ± 2.73 | 32.2 |
| PUK infant serum | 140.5 | 0.5 | 40.9 ± 0.21 | 29.0 |
| | | 1.0 | 42.3 ± 0.29 | 30.0 |
| | | 10.0 | 62.8 ± 1.23 | 41.7 |
| | | 50.0 | 77.3 ± 2.03 | 40.6 |

[b] Content of L-Phe in the sample.

**Table 3** Determination of L-Phe in serum. Determination of L-Phe in adult serum by *D*-CQDs/TCPP ($n=4$)

| Sample | CL[a] (μM) | Added (μM) | Founded (μM) | Recovery (%) |
|---|---|---|---|---|
| Normal serum | 50.5 | 0.5 | 52.04 ± 0.13 | 102.0 |
| | | 1.0 | 50.23 ± 0.25 | 97.5 |
| | | 10.0 | 57.26 ± 0.48 | 94.6 |
| | | 50.0 | 102.54 ± 1.26 | 102.0 |
| PUK patient serum | 1000.5 | 0.5 | 987.21 ± 0.11 | 98.6 |
| | | 1.0 | 1032.18 ± 0.25 | 103.1 |
| | | 10.0 | 1001.29 ± 0.38 | 99.1 |
| | | 50.0 | 1024.48 ± 1.87 | 97.5 |

[a] Content of L-Phe in the sample.

**Table 4** Determination of L-Phe in infant serum. Determination of L-Phe in infant serum by *D*-CQDs/TCPP ($n=4$)

| Sample | CD[b] (μM) | Added (μM) | Founded (μM) | Recovery (%) |
|---|---|---|---|---|
| Normal infant serum | 40.3 | 0.5 | 38.97 ± 0.18 | 95.5 |
| | | 1.0 | 40.01 ± 0.34 | 96.9 |
| | | 10.0 | 51.27 ± 0.41 | 102.0 |
| | | 50.0 | 87.81 ± 1.58 | 97.2 |
| PUK infant serum | 140.5 | 0.5 | 134.29 ± 0.14 | 95.2 |
| | | 1.0 | 144.91 ± 0.31 | 102.4 |
| | | 10.0 | 146.22 ± 1.08 | 97.2 |
| | | 50.0 | 184.56 ± 1.76 | 96.9 |

[b] Content of L-Phe in the sample.

## Conclusions

In conclusion, using two different configurations of chiral CQDs as templates, two configurations of self-assembled chiral materials were prepared by inducing self-assembly of TCPP on *L*-CQDs and *D*-CQDs through non-covalent forces. *L*-CQDs/TCPP and *D*-CQDs/TCPP were used to construct chiral electrochemical sensing interfaces and identify Phe isomers. The results of electrochemical chiral recognition show that *L*-CQDs/TCPP has an effect on D-Phe and *D*-CQDs/TCPP has an effect on L-Phe, which means that *L*-CQDs/TCPP vs D-Phe, *D*-CQDs/TCPP vs L-Phe can form relatively stable diastereomers, thus obtaining a relatively obvious recognition effect. In order to obtain better recognition effect, we optimized the experimental conditions. In addition, the peak current at different concentrations is also tested. With the increase of concentration, the peak current is directly proportional to the concentration, *L*-CQDs/TCPP and *D*-CQDs/TCPP can also detect L-Phe and D-Phe in actual samples. This suggests that the chiral sensing interface induced by self-assembly holds promise for practical applications. Overall, it indicates that the synthesis of chiral composites induced by chiral templates is also an effective way to construct chiral sensing interfaces. Chiral composites synthesized by self-assembly have great potential for electrochemical recognition of chiral biomolecules.

**Supplementary Information** The online version contains supplementary material available at https://doi.org/10.1007/s00604-022-05629-3.

**Funding** This work was supported by the National Nature Science Foundations of China (Grant Nos. 21867015, 22065021), the Key Research Program of Gansu Province (21YF5GA076), the Province Nature Science Foundations of Gansu (Grant Nos. 20JR5RA453, 21JR7RA213), Lanzhou Talent Innovation and Entrepreneurship Project (Grant Nos. 2022-RC-33), Hongliu Outstanding Youth Teacher Cultivate Project of Lanzhou University of Technology and Hongliu Excellent Youth Teacher Cultivate Project of Lanzhou University of Technology.

## Declarations

**Conflict of interest** The authors declare no competing interests.

## References

1. Gal J (2017) Pasteur and the art of chirality. Nat Chem 9:604–605. https://doi.org/10.1038/nchem.2790
2. Hamase K, Morikawa A, Zaitsu K (2002) D-Amino acids in mammals and their diagnostic value. J Chromatogr B 781:73–91. https://doi.org/10.1016/s1570-0232(02)00690-6
3. Genchi G (2017) An overview on D-amino acids. Amino Acids 49:1521–1533. https://doi.org/10.1007/s00726-017-2459-5
4. Tang Y, Cohen AE (2010) Optical chirality and its interaction with matter. Phys Rev Lett 104:163901. https://doi.org/10.1103/physrevlett.104.163901
5. Wang X, Wu J, Liu X, Qiu X, Cao L, Ji Y (2022) Enhanced chiral recognition abilities of cyclodextrin covalent organic frameworks

via chiral/achiral functional modification. ACS Appl Mater Interfaces. https://doi.org/10.1021/acsami.2c05572
6. Zhu G, Kingsford OJ, Yi Y, Wong K-Y (2019) Recent advances in electrochemical chiral recognition. J Electrochem Soc 166:H205. https://doi.org/10.1149/2.1121906jes
7. Miles AJ, Wallace BA (2016) Circular dichroism spectroscopy of membrane proteins. Chem Soc Rev 45:4859–4872. https://doi.org/10.1039/c5cs00084j
8. Wu T, Li G, Kapitán J, Kessler J, Xu Y, Bouř P (2020) Two spectroscopies in one: interference of circular dichroism and Raman optical activity. Angew Chem Int Ed 59:21895–21898. https://doi.org/10.1002/anie.202011146
9. Ma Y, Li Y, Ma K, Wang Z (2018) Optical colorimetric sensor arrays for chemical and biological analysis, Science China. Chemistry 61:643–655. https://doi.org/10.1007/s11426-017-9224-3
10. M.L. Marina Alegre, M. Castro Puyana, S. Bernardo Bermejo, E. Sánchez López (2020) Chiral capillary electrophoresis. https://doi.org/10.1016/j.trac.2020.115807
11. Adam V, Vaculovicova M (2017) Capillary electrophoresis and nanomaterials–Part I: capillary electrophoresis of nanomaterials. Electrophoresis 38:2389–2404. https://doi.org/10.1002/elps.201700097
12. Bao L, Chen X, Yang B, Tao Y, Kong Y (2016) Construction of electrochemical chiral interfaces with integrated polysaccharides via amidation. ACS Appl Mater Interfaces 8:21710–21720. https://doi.org/10.1021/acsami.6b07620
13. Ward TJ, Baker BA (2008) Chiral separations. Anal Chem 80:4363–4372. https://doi.org/10.1021/ac202892w
14. Yi Y, Zhang D, Ma Y, Wu X, Zhu G (2019) Dual-signal electrochemical enantiospecific recognition system via competitive supramolecular host–guest interactions: the case of phenylalanine. Anal Chem 91:2908–2915. https://doi.org/10.1021/acs.analchem.8b05047
15. Wang F, Ji W, Yang P, Feng C-L (2019) Inversion of circularly polarized luminescence of nanofibrous hydrogels through co-assembly with achiral coumarin derivatives. ACS Nano 13:7281–7290. https://doi.org/10.1021/acsnano.9b03255
16. Liu GF, Zhu LY, Ji W, Feng CL, Wei ZX (2016) Inversion of the supramolecular chirality of nanofibrous structures through co-assembly with achiral molecules. Angew Chem Int Ed 55:2411–2415. https://doi.org/10.1002/anie.201510140
17. Wu S, Ye Q, Wu D, Tao Y, Kong Y (2020) Enantioselective recognition of chiral tryptophan with achiral glycine through the strategy of chirality transfer. Anal Chem 92:11927–11934. https://doi.org/10.1021/acs.analchem.0c02335
18. Georgakilas V, Tiwari JN, Kemp KC, Perman JA, Bourlinos AB, Kim KS et al (2016) Noncovalent functionalization of graphene and graphene oxide for energy materials, biosensing, catalytic, and biomedical applications. Chem Rev 116:5464–5519. https://doi.org/10.1021/acs.chemrev.5b00620
19. Zhang Y, Hu L, Sun Y, Zhu C, Li R, Liu N et al (2016) One-step synthesis of chiral carbon quantum dots and their enantioselective recognition. RSC Adv 6:59956–59960. https://doi.org/10.1039/c6ra12420h
20. Wei Y, Chen L, Wang J, Liu X, Yang Y, Yu S (2019) Investigation on the chirality mechanism of chiral carbon quantum dots derived from tryptophan. RSC Adv 9:3208–3214. https://doi.org/10.1039/c8ra09649j
21. Chatterjee T, Shetti VS, Sharma R, Ravikanth M (2017) Heteroatom-containing porphyrin analogues. Chem Rev 117:3254–3328. https://doi.org/10.1021/acs.chemrev.6b00496
22. Ding Y, Zhu W-H, Xie Y (2017) Development of ion chemosensors based on porphyrin analogues. Chem Rev 117:2203–2256. https://doi.org/10.1021/acs.chemrev.6b00021
23. Higashino T, Yamada T, Sakurai T, Seki S, Imahori H (2016) Fusing porphyrins and phospholes: synthesis and analysis of a phosphorus-containing porphyrin. Angew Chem Int Ed 55:12311–12315. https://doi.org/10.1002/anie.201607417
24. Fujimoto K, Oh J, Yorimitsu H, Kim D, Osuka A (2016) Directly diphenylborane-fused porphyrins. Angew Chem Int Ed 55:3196–3199. https://doi.org/10.1002/anie.201511981
25. Zhao L, Qu R, Li A, Ma R, Shi L (2016) Cooperative self-assembly of porphyrins with polymers possessing bioactive functions. Chem Commun 52:13543–13555. https://doi.org/10.1039/c6cc05449h
26. Sugimoto T, Suzuki T, Shinkai S, Sada K (2007) A double-stranded helix by complexation of two polymer chains with a helical supramolecular assembly. J Am Chem Soc 129:270–271. https://doi.org/10.1021/ja067613h
27. Choi J, Wagner P, Jalili R, Kim J, MacFarlane DR, Wallace GG et al (2018) A porphyrin/graphene framework: a highly efficient and robust electrocatalyst for carbon dioxide reduction. Adv Energy Mater 8:1801280. https://doi.org/10.1002/aenm.201801280
28. Shin JY, Yamada T, Yoshikawa H, Awaga K, Shinokubo H (2014) An antiaromatic electrode-active material enabling high capacity and stable performance of rechargeable batteries. Angew Chem 126:3160–3165. https://doi.org/10.1002/anie.201310374
29. Park JM, Lee JH, Jang W-D (2020) Applications of porphyrins in emerging energy conversion technologies. Coord Chem Rev 407:213157. https://doi.org/10.1016/j.ccr.2019.213157
30. Wu S, Yin Z-Z, Wu D, Tao Y, Kong Y (2019) Chiral enantioselective assemblies induced from achiral porphyrin by L-and D-lysine. Langmuir 35:16761–16769. https://doi.org/10.1021/acs.langmuir.9b03255
31. Burgard P, Ullrich K, Ballhausen D, Hennermann JB, Hollak CE, Langeveld M et al (2017) Issues with European guidelines for phenylketonuria. Lancet Diabetes Endocrinol 5:681–683. https://doi.org/10.1016/s2213-8587(17)30201-2
32. Blau N, Van Spronsen FJ, Levy HL (2010) Phenylketonuria. The Lancet 376:1417–1427. https://doi.org/10.1016/s0140-6736(10)60961-0